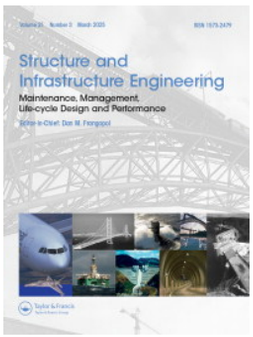

Taylor & Francis
Taylor & Francis Group

Structure and Infrastructure Engineering
Maintenance, Management, Life-Cycle Design and Performance

ISSN: (Print) (Online) Journal homepage: www.tandfonline.com/journals/nsie20

Full scale test on reinforced concrete elements of an existing bridge: on-site investigation and laboratory testing design

Diego Talledo, Gianluca Bottin, Luca Pozza, Luisa Berto, Nicola Buratti, Marco Savoia & Anna Saetta

To cite this article: Diego Talledo, Gianluca Bottin, Luca Pozza, Luisa Berto, Nicola Buratti, Marco Savoia & Anna Saetta (15 Jan 2025): Full scale test on reinforced concrete elements of an existing bridge: on-site investigation and laboratory testing design, Structure and Infrastructure Engineering, DOI: 10.1080/15732479.2024.2446725

To link to this article: https://doi.org/10.1080/15732479.2024.2446725

Published online: 15 Jan 2025.

STRUCTURE AND INFRASTRUCTURE ENGINEERING
https://doi.org/10.1080/15732479.2024.2446725

Full scale test on reinforced concrete elements of an existing bridge: on-site investigation and laboratory testing design

Diego Talledo[a], Gianluca Bottin[a], Luca Pozza[b], Luisa Berto[a], Nicola Buratti[b], Marco Savoia[b] and Anna Saetta[a]

[a]Department DCP, University IUAV of Venezia, Venezia, Italy; [b]Department of Civil, Chemical, Environmental and Materials Engineering, University of Bologna, Bologna, Italy

ABSTRACT

The evaluation of mechanical characteristics and degradation level of existing bridges is a highly relevant topic today. This paper presents the initial phases of an integrated experimental-numerical research project focused on a pre-scheduled demolition of an existing reinforced concrete bridge. The controlled demolition of existing bridges represents an invaluable opportunity, allowing to deepen our comprehension on their behavior, especially when degradation analysis is concerned. Both on-site tests and subsequent laboratory experiments design are carried out on full-scale elements extracted from the bridge. These tests are complemented by Finite Element analyses conducted at various levels of detail. Specifically, after the description of the knowledge phases of the bridge performed on-site, the paper illustrates the preliminary numerical analyses carried out to support the customized design of the experimental setup, where mean values of all material parameters are assumed to acquire the essential information on the expected test results. Additionally, Monte Carlo analysis has been performed to evaluate the impact of statistical variability of material parameters on structural response. This aspect is particularly relevant for the design of the experimental test setup, due to the large forces involved and large displacements expected in order to reach the full collapse of the beams.

ARTICLE HISTORY
Received 22 April 2024
Revised 29 July 2024
Accepted 1 September 2024

KEYWORDS
Degradation; existing RC bridges; FE analyses; full scale tests; laboratory tests; Monte Carlo simulations; on-site tests

1. Introduction

The degradation of existing reinforced concrete bridges has become an emerging problem in many countries, with significant implications in terms of infrastructure safety. For instance, (Žnidarič, Pakrashi, O'Brien, & O'Connor, 2011) reports the results of a review on road structure data in six European countries (Slovenia, Poland, Hungary, Czech Republic, Austria, Norway) showing that the majority of their bridges were built between 1900 and 1980, with a peak in the construction rate between 1946 and 1965. Similar data can be found in the deliverable '*D1.2 European Railway Bridge Demography*' of the Sustainable Bridges European project, which reports the results of an analysis on 1800 railway bridges carried out in 2004; 55% of the concrete bridges investigated were between 20 and 50 years old and 20% were more than 50 years old. As far as US is concerned, according to ASCE (ASCE, 2021), there are about 617,000 highway bridges in the US, 42% of which are at least 50 years old and 12% are aged at least 80 years. Furthermore, 46154 bridges are considered structurally deficient. On these aged infrastructures, the combination of aging, environmental factors, and increasing loads have resulted in severe structural deterioration (Bencivenga et al., 2022), which in some cases has led to structural failures with fatalities (Calvi et al., 2019; Deng, Wang, & Yu, 2016).

For the aforementioned reasons, recently, there has been a growing global research effort to define procedures and methods for assessing the residual capacity of existing infrastructures, especially those that come closer or surpass their expected service life. In Italy, these procedures have been included into a comprehensive multi-hazard and multi-level risk assessment framework for existing bridges, introduced by the document '*Guidelines for classification and risk management, safety assessment, and structural health monitoring of existing bridges*' issued by the National Ministry for Infrastructures and Transportation (MIT, 2020). These Guidelines represent a significant advancement in the regulatory framework for existing bridges, as outlined by Cosenza and Losanno (2021).

Clearly, a robust assessment of the degradation of materials and of their residual mechanical properties is crucial for the safety assessment of existing bridges, however, in some cases it may not be sufficient to obtain reliable estimates of the structural capacity due to limitations in structural analysis models. Specifically, studies examining the structural effects of degradation processes in natural environments necessitate further investigation. Consequently, numerous national-level research projects are focused on testing the behavior of actual structural elements extracted from bridges and viaducts scheduled for demolition. The controlled demolition of existing bridges, beyond its pragmatic purpose, represents an invaluable opportunity to enhance knowledge regarding existing infrastructures, particularly

CONTACT Diego Talledo diego.talledo@iuav.it Department DCP, University IUAV of Venezia, Dorsoduro 2206, Venezia 30123, Italy.

with reference to degradation analysis. It facilitates an in-depth exploration of potentialities of diagnostic techniques and the evaluation of residual load-bearing capacity.

Most of the research initiatives documented in publications have been focused on Prestressed reinforced Concrete (PC) bridge beams, due to their widespread adoption in transportation infrastructures, their limited ductility and high sensitivity to deterioration of prestressing steel elements and to pre-stress losses (Bagge, Popescu, & Elfgren, 2018). Shenoy and Frantz (1991) tested to failure two 27-year-old PC box beams, removed from a deteriorated multi-beam bridge. Halsey and Miller (1996) tested two 40-year-old inverted T-beams decommissioned from a bridge and compared their behavior with that of prototype beams tested at the time of construction of the bridge. Pessiki, Kaczinski, and Wescott (1996) presented the results of an experimental campaign aimed at evaluating the effective prestress force in two full-scale PC bridge beams, removed from a bridge after 28 years in service. Eder, Miller, Baseheart, and Swanson (2005) tested two 50-year-old, post-tensioned PC girders to evaluate their ultimate load capacity. Taffe, Hillemeier, and Walther (2010) performed tests on 19 decommissioned PC bridge beams; both nondestructive and destructive flexural tests were carried out and their results were compared.

Papé and Melchers (2011) tested three PC beams from a 45-year-old bridge, and observed severe strength and ductility reductions in beams affected by corrosion and concrete deterioration. Rogers, Wotherspoon, Scott, and Ingham (2012) reported the results of an extensive testing campaign on 19 decommissioned PC beams extracted from a bridge, some of which were affected by chloride induced corrosion. The beams affected by corrosion were found to have a strength reduction of 31% compared to beams in good condition. Bagge et al. (2015) carried out failure loading tests on the girders and the deck on at 55-year-old post-tensioned PC bridge. Liu and Jia (2019) conducted tests and non-linear finite element analysis for four beams which served for 20 years in an area affected by freezing-thaw cycles. Wang, Tang, Zheng, Zhou, and Zhu (2020) tested a full scale pre-stressed box girder and developed an analysis model based on the finite strip method. Jeon, Sim, and Shim (2021) tested full-size deteriorated 45-year-old PC bridge girders recovered from an existing bridge, to investigate their cracking, yielding and ultimate strength.

Savino et al. (2023) presented the results of tests on a set of four 50-year-old PC bridge girders, recovered from a decommissioned bridge. Tests were carried out using a specifically designed steel reaction frame. Tonelli et al. (2023) presented a comparison between the response of PC bridge subjected to a controlled load test up to its failure, with the predictions obtained by means of four different structural models. Losanno, Galano, Parisi, Pecce, and Cosenza (2024) investigated form an experimental and analytical point of view the nonlinear flexural behavior of post-tensioned concrete bridge girders with different grouting conditions and prestress levels. Studies involving tests on cast-in-situ Reinforced Concrete (RC) structural elements from aged road infrastructures are more limited (Jiang et al., 2023; Lantsoght, Yang, van der Veen, de Boer, & Hordijk, 2016; Miller, Aktan, & Shahrooz, 1994).

The main limitation of many experimental studies on large beams is due to the fact that large displacements are usually possible before attaining the actual beam collapse, and often tests are stopped due to test setup limitations, so not allowing for a correct detection of the actual ductility of the RC element. However, experimental data on the performance of these elements are crucial for appropriately calibrating numerical models capable of predicting the life-cycle structural performance of RC bridge elements.

The current work presents the preliminary results of a hybrid numerical-experimental research project, involving the University IUAV of Venice and the University of Bologna, concerning the Fratta River bridge in Valli Mocenighe, Piacenza d'Adige (PD) in Northern Italy, an approximately 80-year-old RC structure. The bridge was decommissioned as a part of a broad road system renewal initiative and replaced with a new mixed steel-concrete structure. After a description of the features of the bridge and of the necessary steps to attain an adequate level of knowledge, the paper presents the outcomes of preliminary numerical analyses conducted to simulate the behavior of the bridge's primary beams. These analyses are aimed to design a specific experimental setup for a future testing of the beams up to failure. Then, the results of Monte Carlo simulations are presented in order to assess the role of uncertainties regarding the mechanical properties of materials on the structural behavior of the beams.

The proposed comprehensive approach ensures a thorough understanding of the experimental conditions and of the potential effects of material property variations on the structural behavior. Concerning the effect of natural corrosion on the ultimate behavior of RC beam, one of the main aims of the propsed experimental campaign is to evaluate possible changes in the failure mode of the RC beam as the level of natural corrosion increases. As an example, a more pronounced corrosion of the transverse reinforcement (stirrups) can cause the failure mode to shift from bending to shear.

2. The 'Fratta' bridge

The 'Fratta' bridge is located in the northeast of Italy near Piacenza d'Adige, Figure 1. The bridge crosses the Fratta River with an angle of inclination of approximately 10 degrees, so producing a skewed geometry of the bridge deck. As frequently occurs in the case of old bridges, there is a lack in available documentary information, and the structural project of the bridge is unavailable. Only few original drawings have been found, some of them are depicted in Figure 2. As indicated by the project cover page, the bridge was designed in 1948. The limited availability of historical data (lack of project details, drawings, and calculation reports) makes it essential to plan a thorough campaign of tests and investigations with the aim of acquiring a sufficient level of knowledge of the bridge. One of main aims of the ongoing research project led by the University IUAV of

Figure 1. Fratta bridge (Italy): aerial views obtained with the drone survey.

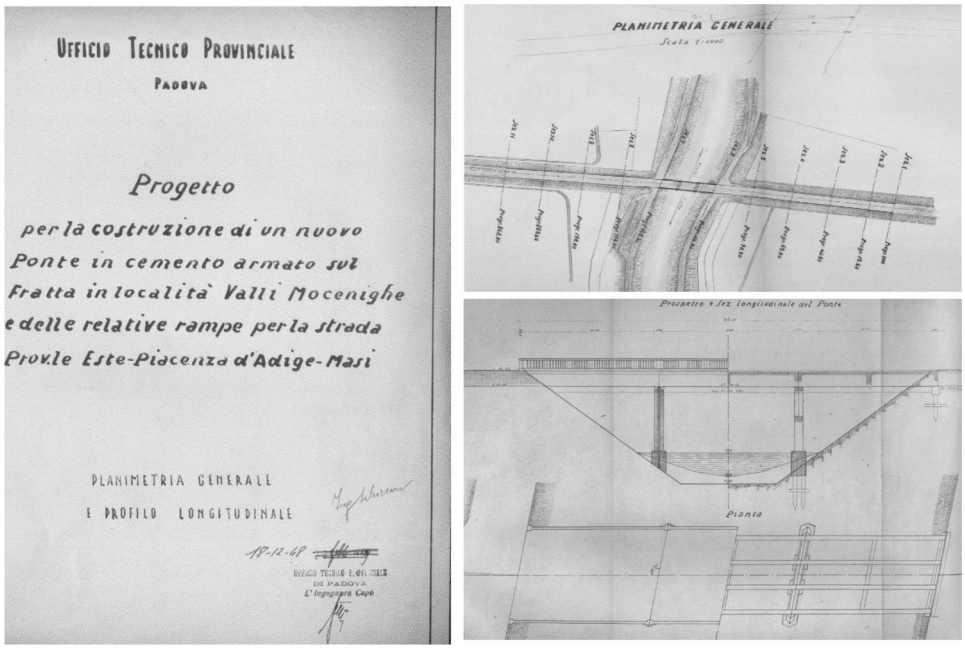

Figure 2. Original drawings of the Fratta bridge project: project cover page; general plan of the site and side and plan view of the bridge.

Venice and the University of Bologna is to take advantage of the opportunity to conduct both on-site tests and laboratory tests on full-scale elements. These tests enable us to assess the reliability of on-site testing in characterizing the bridge as well as assessing how a not artificially induced and well-defined degradation level (i.e. directly measurable) impacts the structural elements response until failure.

The research activities conducted up to now on the Fratta bridge are structured in two phases:

- Phase 1 – in situ test and investigation: a series of preliminary activities conducted before the dismantling of the bridge in order to acquire a general overview on the geometry, the constructive details, the materials, the conservation state of the existing structure. These activities started carrying out a geometrical survey using the laser scanner technique and a drone survey, which allowed to acquire information and images to draw up the degradation maps of the individual structural elements. In addition, visual inspection was carried out compiling the 'defect forms' provided by the Italian Guidelines (MIT, 2020). Some destructive tests were carried out by sampling concrete cores and steel reinforcing bars and subsequent laboratory characterization. Reinforcement pattern of the existing structure (girders and slab) was traced using metal detector and GPR (Ground Penetrating Radar), e.g. Cheilakou, Theodorakeas, Koui, Moustakidis, and Zeris (2013).
- Phase 2 – design of laboratory tests: detailed design of controlled bridge demolition and subsequent executive design of experimental setup supported by predictive FE numerical simulations.

After the testing phase, to be carried out in the next months, a careful investigation will be carried out on the individual elements tested, aimed at confirming the preliminary evaluations on: reinforcement details, material properties, state of degradation (in particular measuring the corrosion level of steel bars with advanced 3D scanning techniques such as structured-light scanning, e.g. Di Carlo et al. (2023).

2.1. Geometrical survey

The geometry of the bridge was obtained through a detailed laser-scanner survey combined with traditional on-site measurements. The Fratta bridge is constituted by three structurally independent cast on-site RC decks, featuring three simply supported spans, each spanning 12 m. Each span, with a width of 8.10 m, consists of three 1.0 m high beams supporting a 20 cm thick concrete slab. Equidistant RC transverse beams connect the longitudinal girders, with one positioned at the center and two at the ends. The height of the central transverse beam is the same as the longitudinal girders, while the height of the end ones is about 20 cm smaller, to leave the space in height for the supports. The bridge deck is supported by fixed lead sheet bearings. In the riverbed, the piers rise to a height of 5.00 m and are constituted by two RC frames each in the upper part.

The structural joint between the frames (and consequently between the decks) measures approximately 2 cm, serving to accommodate thermal deformations of the span. The abutments, standing at a height of 2.80 m, feature rear and wing walls that incorporate the approach embankment. Piers and abutments foundations are pile driven, although specific details are currently unavailable. Some examples of the geometrical survey outputs are depicted in Figure 3, where the plan, the lateral view and a transversal cross-section of the bridge are represented. Next to the geometrical drawings, the corresponding images obtained from the laser scanner survey are also reported.

In addition, a drone survey was carried out. Surveying with a drone allows to acquire photos of parts of the structure that are not visible or directly reachable by the classical laser scan technique (e.g. parts above the watercourse, supports). It is worth noting that the drone survey turns out to be very effective in terms of diagnostics and degradation mapping of inaccessible structural elements. Figure 4 reports a selection of photos obtained with the drone survey.

2.2. Degradation survey

In parallel with the geometric survey, a degradation survey of the main elements of the bridge was carried out, resulting in a series of graphical drawings and orthophotos that allow a preliminary assessment of the state of degradation of the structure. In particular, the main types of degradation, such as cracking patterns, the presence of efflorescence and biological growth, etc. were highlighted. Figure 5 shows the degradation maps of three longitudinal sections of the bridge. The surfaces of both lateral girders and piers exhibit degradation phenomena due to the synergy effect of aging and exposure to aggressive atmospheric conditions. There is an evident concrete scouring caused by water leakage at the end sections of the lateral girders and the external pillars of the pier. Additionally, a minor corrosive attack is evident along the edges of the elements, featuring limited portions of exposed rebars. Finally, the degradation level of the two

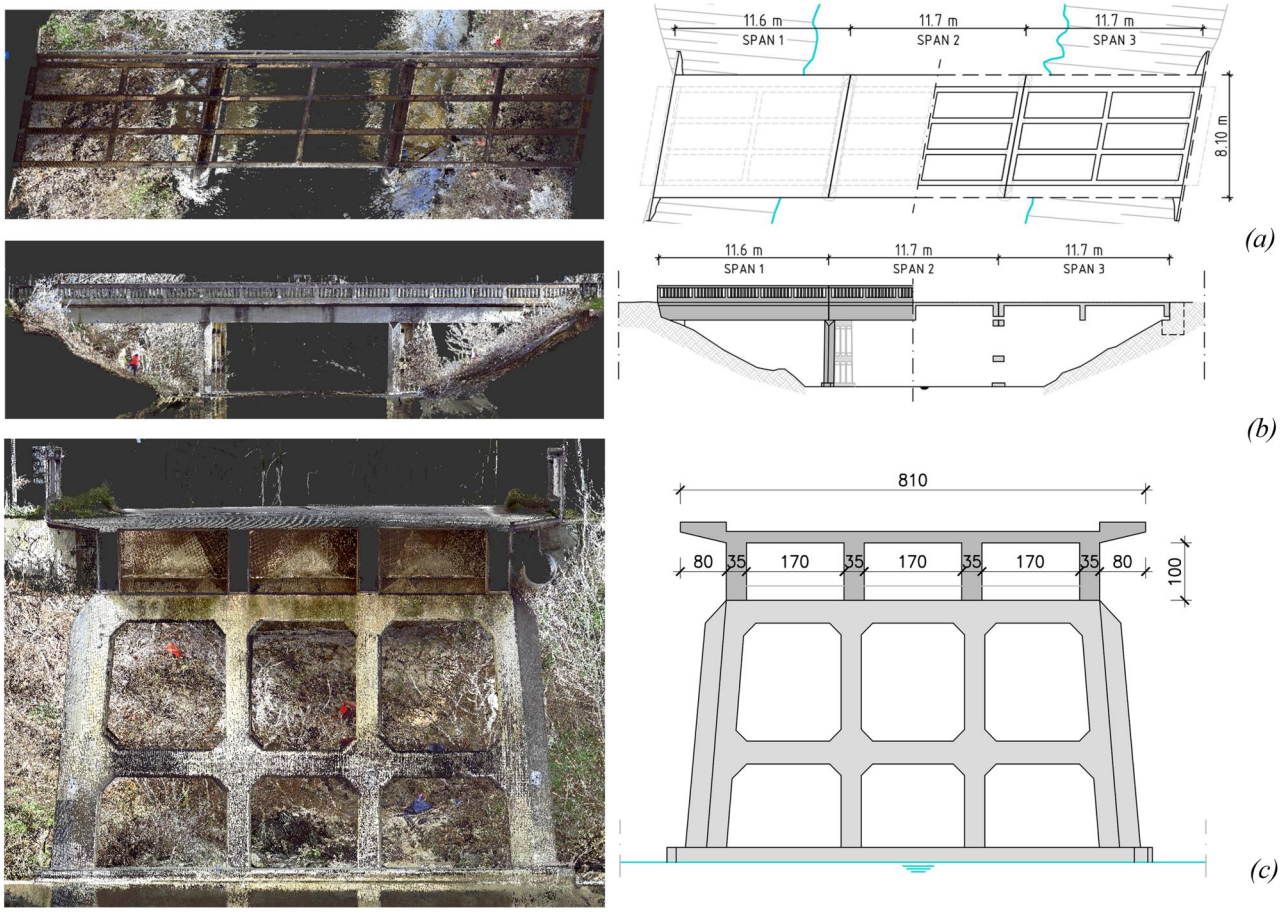

Figure 3. (a) Top view; (b) lateral view; (c) cross-section of the Fratta bridge.

Figure 4. Photos obtained by the drone survey.

external beams is, as expected, significantly more pronounced compared to that of the central beams.

2.3. Rebars survey and material characterization

Due to the lack of original project documentation, especially in terms of structural details, the use of non destructive survey techniques, including metal detectors and Ground Penetrating Radar (GPR) is recommended, to obtain the reinforcement layout of the existing structure (Cheilakou et al., 2013). With reference to the lateral bridge beam, Figure 6a depicts the layout of the reinforcement as reconstructed from the multiple investigations carried out both on-site and on the demolished beams. Figure 6b shows a photo of the reinforcement of the demolished beam, Figure 6c the main cross-sectional views of the beam, and Figure 6d the results of one of the GPR investigations carried out on the beams.

Note that a thorough survey of the reinforcement layout is essential for conducting a reliable predictive assessment of the load bearing capacity of the girders. In this case, the accuracy of the identified layout has been a posteriori validated by comparison with the real reinforcement layout observed in the beams of the demolished spans (Figure 6b). The layout of the reinforcements detected with the nondestructive diagnosis technique was found to be consistent with that obtained by direct inspection after demolition of nearby spans. It is worth noting that the reconstruction of the reinforcement layout, and in particular of the position of diagonal steel bars, may be subjected to inaccuracies due to unavoidable uncertainties in on-site measurements, as well as to the fact that surveys were not replicated and verified by direct inspection on all beams of the bridge.

It is worth noting that, according to the practice of the time, plain bars were used. To characterize the material properties and obtain the most precise input parameters for the FEM model used to design the experimental setup, the following tests were conducted:

- Density measurements and concrete carbonation tests followed by compression tests on eight cylindrical concrete cores with a height to diameter ratio equal to h/d = 2, extracted from the transverse beams and the slab. Additionally the elastic modulus of concrete was measured on four of the eight cores.
- Tension tests on five samples of 14 mm diameter and two samples of 28 mm diameter extracted from longitudinal steel bars.
- Tension tests on seven samples of 8 mm diameter extracted from steel stirrups.

Figure 7a depicts the positioning of the concrete samples along the bridge and Figure 7b some photos of the samples before and after carbonation test. Table 1 lists the geometric dimensions of each specimen, the type of test and the results in terms of compressive strength and elastic modulus. Table 2 summarizes the results of the tension tests carried out on the seven longitudinal reinforcement steel samples (where the value of A_{gt} derives from manual measurement of strain at peak stress) and the seven reinforcement steel samples from stirrups.

3. Design of laboratory test

3.1. Design of the controlled bridge demolition

The deconstruction process of the span on the Piacenza d'Adige side of the Fratta bridge was specifically designed in

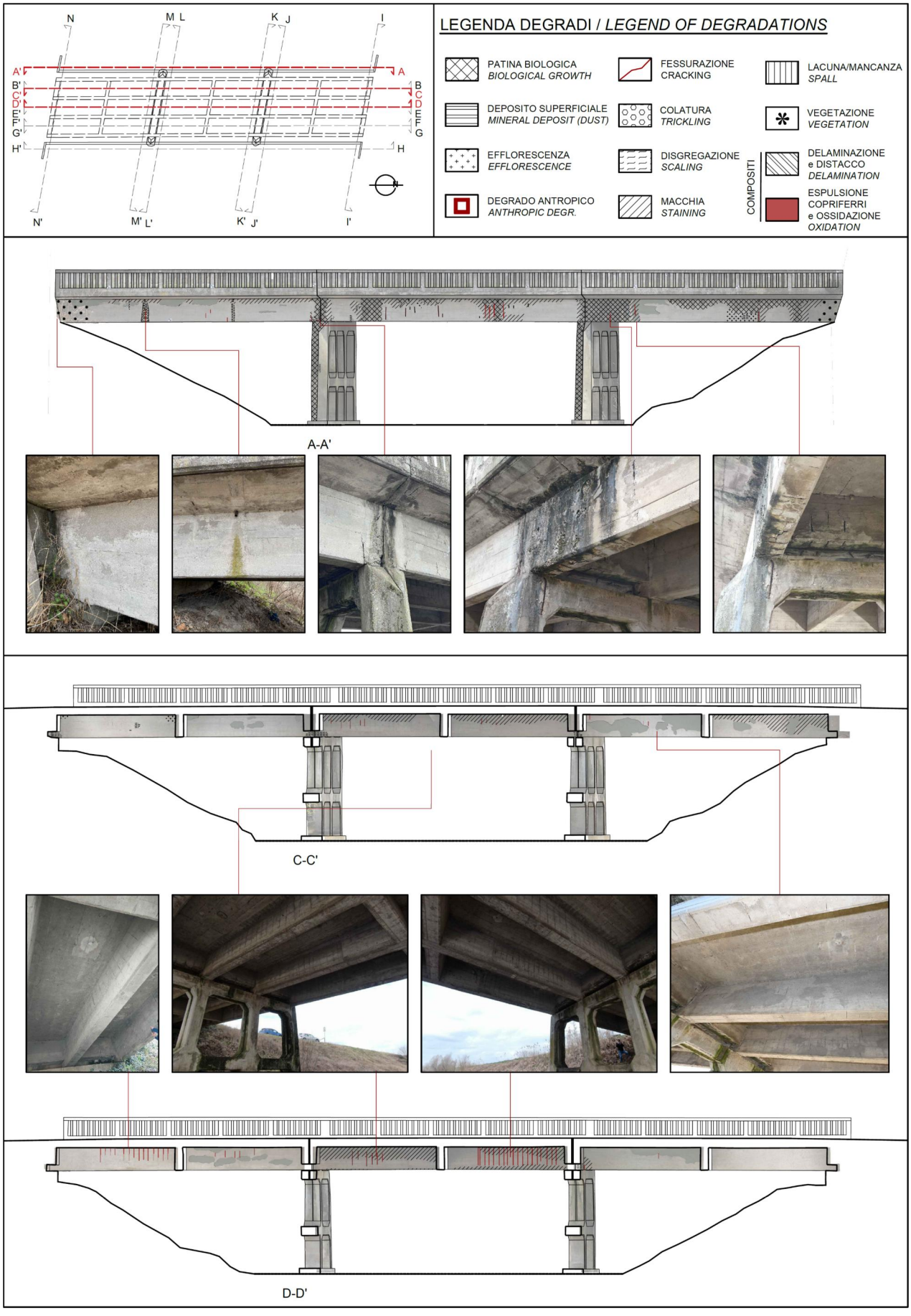

Figure 5. Degradation maps of principal bridge elements.

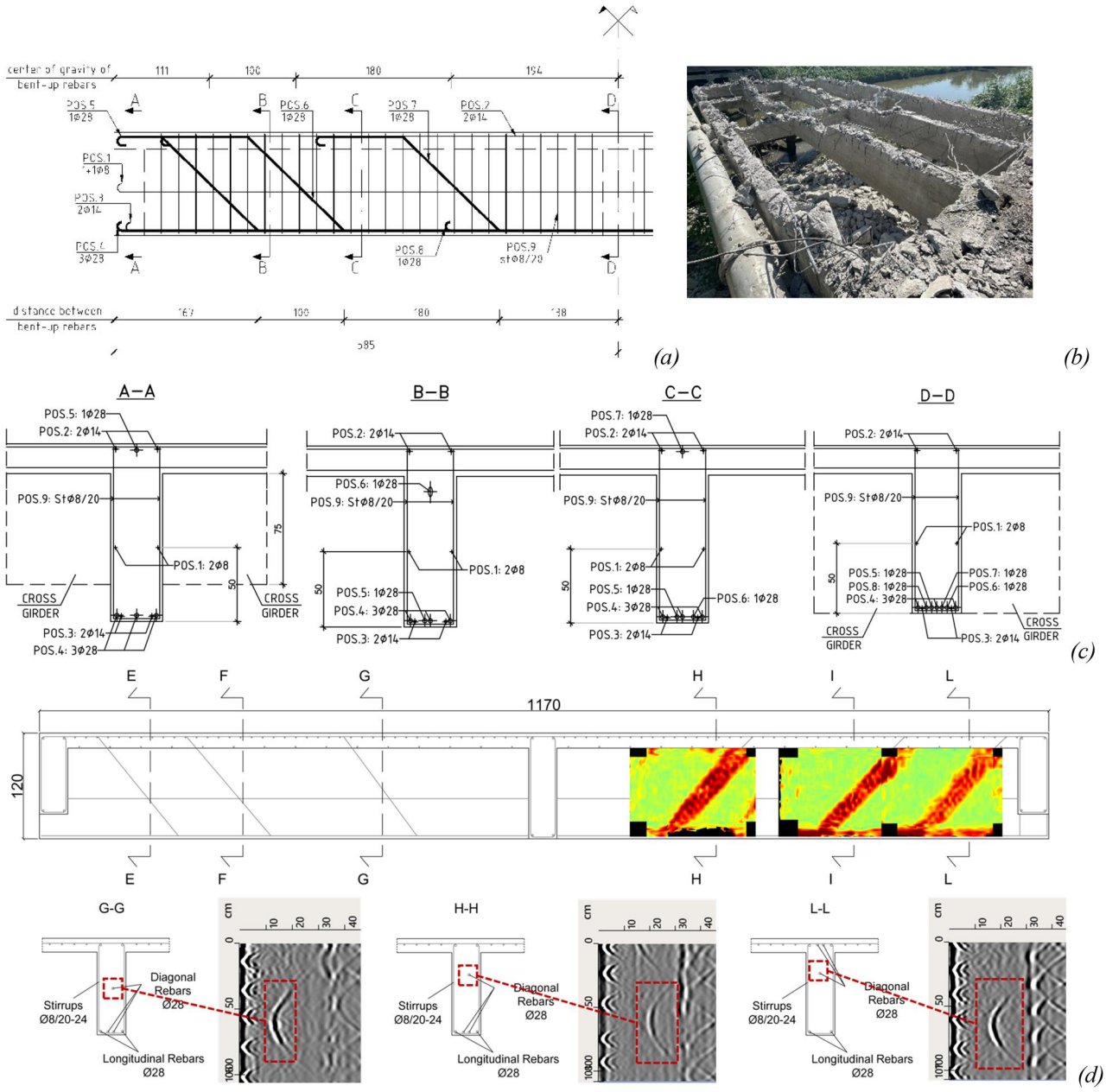

Figure 6. Survey of reinforcement of the lateral bridge beam: a) reinforcement layout; b) photo of reinforcements of the demolished beam; c) cross sections of the beam; d) Ground Penetrating Radar (GPR) results.

order to extract suitable girders to conduct bending tests in the mechanical laboratory of CIRI-EC of University of Bologna. Four girders were extracted from the deck according to the deconstruction scheme represented in Figure 8. The deconstruction process involves: cutting, lifting, transportation and positioning phases, as reported in the photographic sequence of Figure 9.

The transversal adjacent longitudinal girders were separated respecting the red cutting lines depicted in Figure 8. The concrete slab was cut using diamond disks while the end and middle transversal girders were separated by means of controlled demolition (Figure 9b). Resulting beam samples preserved the T-cross section with a representative wing width and were characterized by dimension and weight compatible with the lifting and road transport limits of vehicles. Once the cutting phase was completed, the girders were lifted using a high-capacity mobile crane (Figure 9b). The lifting points of the beams were defined in order to avoid tension forces on the slab, thus avoid its cracking. It is worth nothing that the lifting phase is critical as it stresses the girder with a different static scheme and load pattern compared to the on-site configuration. The relevant weight and dimension of the girders required exceptional transports by truck to move the girders from the bridge site to the laboratory (Figure 9c). Finally, the girders were stored at the structural laboratory of CIRI-EC of University of Bologna (Figure 9d).

3.2. Preliminary design of laboratory test configuration

Starting from the results of the survey phases, regarding both geometry of the beam and details of the longitudinal

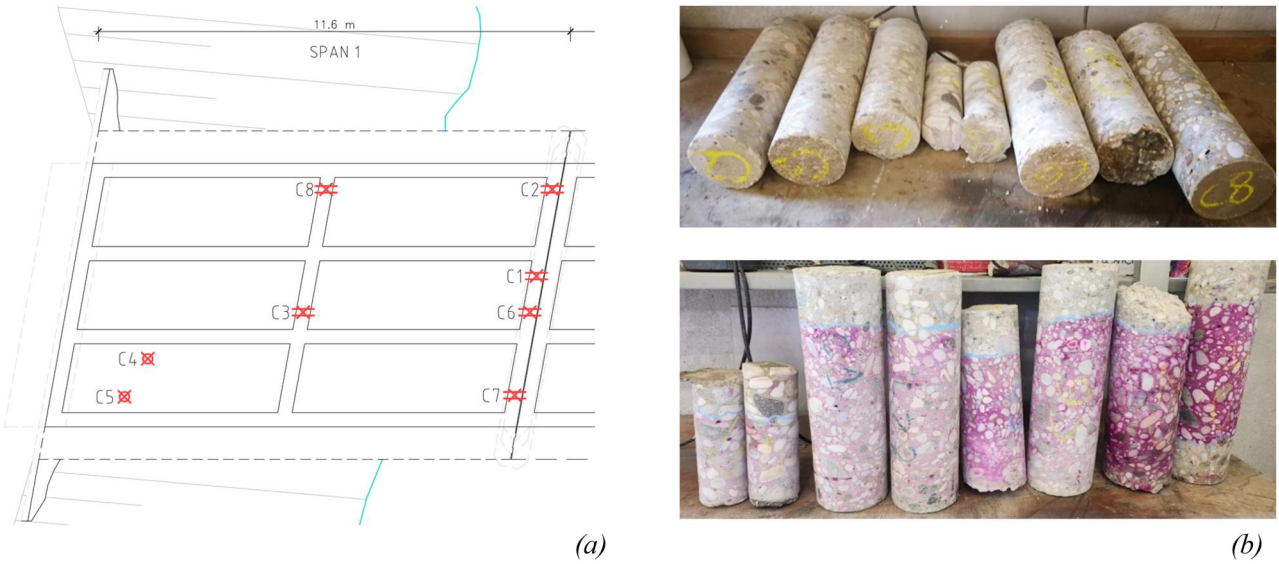

Figure 7. (a) Sampling points for concrete specimens along the bridge; (b) photos of the specimens.

Table 1. Mechanical properties of concrete specimens from slab and girders estimated from laboratory tests.

Concrete specimen ID	Diameter [mm]*	Compressive strength f_c [MPa]	Elastic modulus E_c [MPa]
C1	99.40	35.3	–
C2	95.81	26.2	–
C3	95.98	31.8	–
C4	63.00	22.0	36,650
C5	64.21	40.8	–
C6	101.00	31.3	34,372
C7	104.53	31.3	43,654
C8	104.51	20.5	33,888

*mean value of three measures.

Table 2. Mechanical properties of steel specimens.

Steel specimen ID	Diameter [mm]*	Ultimate strain A_{gt} [%]	Yield strength f_y [MPa]	Ultimate strength f_t [MPa]	Elastic modulus E [MPa]
ϕ14-I	14.08	30.41	355.6	448.7	170,573
ϕ14-II	14.40	32.57	350.8	467.3	239,176
ϕ14-III	14.24	25.41	448.6	689.8	224,903
ϕ14-IV	13.97	21.28	406.8	514.8	240,060
ϕ14-V	13.94	–	348.1	481.7	208,900
ϕ28-I	26.95	–	304.1	439.2	–
ϕ28-II	26.93	–	317.5	430.9	–
ϕ8–I	7.42	13.23	313.4	381.7	210,755
ϕ8–II	7.74	10.47	286.8	354.4	
ϕ8–III	7.89	23.45	319.8	444.9	222,456
ϕ8 – IV	7.79	23.76	379.1	469.6	
ϕ8 – V	7.76	–	294.3	356.6	
ϕ8 – VI	7.83	–	252.0	341.6	
ϕ8 – VII	7.74	40.93	328.9	460.6	

*mean value of three measures.

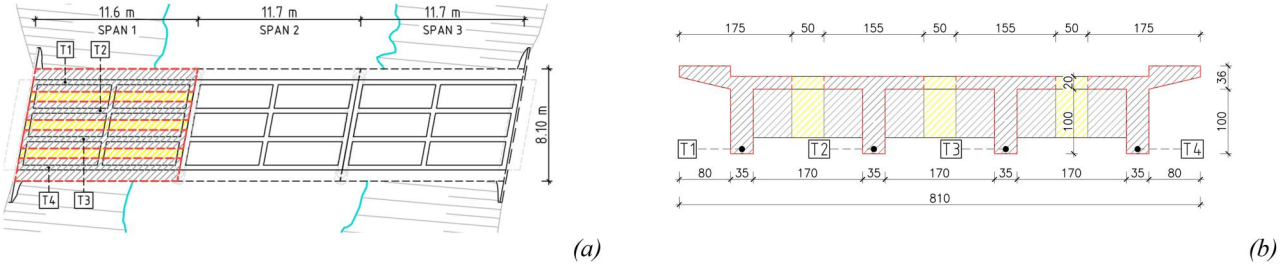

Figure 8. Deconstruction scheme with the indication of the cutting lines for the end span: (a) plan view; (b) cross section.

and transversal reinforcements, the test configuration to be carried out in the laboratory has been defined. A four-point bending test has been selected, for which the loads distance a has been set in order to maximize the probability of inducing flexural failure, Figure 10. The purpose of ensuring as much as possible that a flexural failure occurs in the

Figure 9. Main phases of the demolition process: (a) cutting of the slab and demolition of the transverse beams; (b) lifting of the girders; (c) loading the beams onto the truck bed; (d) positioning of the girders at the CIRI-EC structural testing laboratory of the University of Bologna.

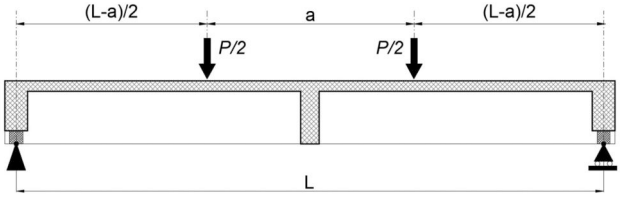

Figure 10. Four-point bending test scheme, where the span is $L = 11.35$ m and a is a variable parameter.

slightly degraded central beam, matches with the objective of investigating the effect of natural corrosion on the failure mode of the beams. Actually, if the experimental set-up is designed to attain a bending failure of the central beam, when the more degraded edge beam is tested, a variation in the failure mode from bending to shear can be observed, depending on the corrosion level of the superficial transverse reinforcement (stirrups).

The arrangement of the reinforcing bars and the presence of inclined rebars (i.e. diagonal bar) make it not immediately straightforward to predict the sections where failure will occur as a function of the distance between the loading points. An analytical model has then been adopted where both flexural and shear failure have been considered.

The analytical model for flexure is based on sectional analysis, assuming plane sections, adopting parabola-rectangle constitutive law for concrete and elastic-perfectly-plastic law for steel. For the evaluation of bending strength, numerical integration by means of discretization of the section into fibers has been applied. Concerning the bond behavior, to account for the adoption of plain rebars, the point at which the bar is considered active has been shifted to account for an adeguate transfer length.

For what concerns shear strength, considering the presence of both stirrups and diagonal bars, the well-known truss model has been adopted (e.g. CEN, 2015; MIT, 2018). As widely known, according to this model, the shear resistance depends on the inclination of the compression strut (generally indicated with angle θ) ranging from 45 to 21.8 degrees corresponding to a cotangent value of θ variable from 1 to 2.5. A value of cotangent of 1 may lead to a very conservative estimation of the shear strength, on the other hand, moving toward higher values of cotangent, the failure of the compression strut may precede the failure of the tensile diagonal of the truss. In the considered case, even with the minimum angle θ = 21.8 degrees, the shear failure occurs due to diagonal steel failure long before the concrete compression failure. This may permit to adopt high value of cotangent; nevertheless, it is worth noting that the aim of this analysis is to design a test setup with a reduced probability of attaining shear failure; therefore, a conservative estimate of shear resistance, adopting lower values of cotangent, was considered. In particular, a value of cotangent equal to 1.5 has been selected in this study, according to experimental tests conducted on beams of similar span and height (Täljsten, Nilimaa, Blanksvärd, & Sas, 2011) where a crack inclination of approximately 32 degrees, corresponding to a cotangent of about 1.6, have been observed.

The material parameters adopted in the analysis are based on the material characterization tests reported in the previous section. In particular, as a first analysis, the mean values of concrete strength ($f_c = 29.89$ MPa) and yield strengths for the different bar diameters ($f_{y,8} = 310.6$ MPa, $f_{y,14} = 381.98$ MPa, $f_{y,28} = 310.8$ MPa respectively for 8, 14 and 28 mm) are assumed. The resisting moment and the resisting shear along the beam are depicted respectively in shaded grey and red colors in Figures 11 and 12. In Figure 11a,b, for the sake of comparison, these capacities are superimposed with internal forces (moment and shear) from traffic loads provided by Italian

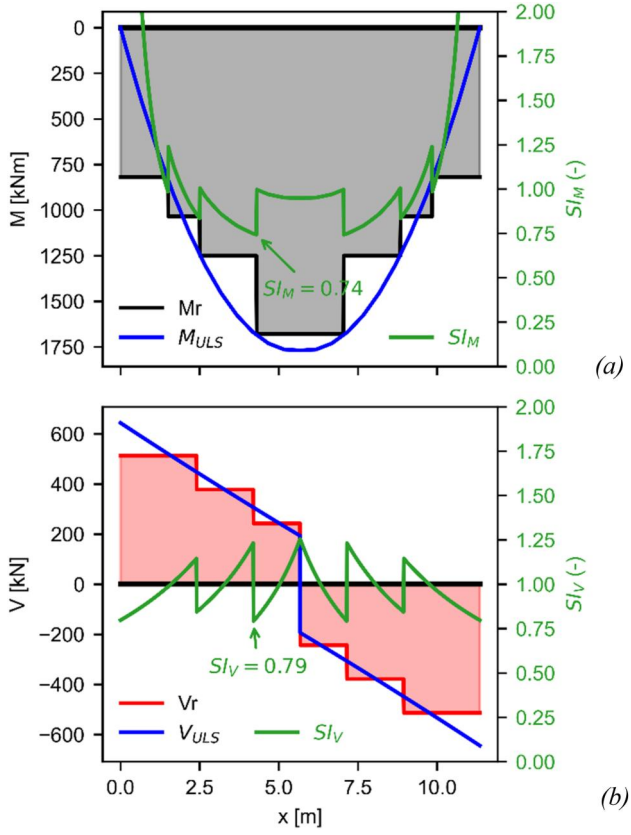

Figure 11. Distribution along the beam of resisting and acting: a) moment; b) shear. Acting moment and shear are computed with reference to provided traffic actions by Italian code (MIT, 2018) at ultimate Limit state. The green lines represent respectively the safety index for moment (SI_M) and shear (SI_V) computed as the ratio between capacity and demand. The minimum safety index is indicated by green arrow.

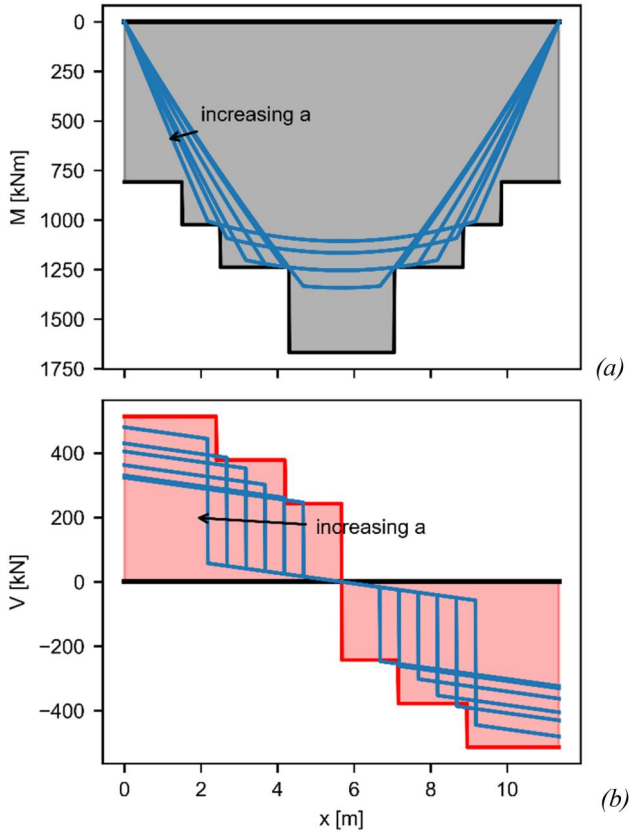

Figure 12. Distribution along the beam of resisting and acting: a) moment; b) shear. Acting moment and shear are evaluated as a function of the load leading to flexural failure for different distance *a* between the forces: 2, 3, 4, 5, 6 and 7 m.

Code (MIT, 2018) at Ultimate Limit State. The same figure depict the safety index evaluated as the ratio between capacity and demand. As it can be seen the minimum safety index corresponds to a flexural failure in the central portion of the beam.

On the other hand, with the aim of simulating the experimental setup, in Figure 12 the superimposed blue curves represent the internal forces for increasing distance *a* between the loads (i.e. 2 to 7 m, corresponding to a shear-span-to-depth ratio about between 4 to 2), and for load values equal to those leading the flexural failure (in some section of the beam). When the applied shear force is higher than the resisting shear, a shear failure is expected, while in the other cases a flexural failure is expected. It is possible to observe that a shear failure is expected for 2 and 6 meters of distance between the forces. This can be better evidenced looking at Figure 13a, where the ultimate loads for both flexural and shear failures are depicted as a function of distance between the loads.

Two discontinuity points can be evidenced for shear strength, due to the reinforcement layout of diagonal bars; it is worth noting that a small uncertainty in their position can strongly affect the shear strength. A shift of 5 cm in the position of the diagonal bar (Pos.7 in Figure 6a) toward the support, named 'shifted case' in Figure 13b, can lead to a shear failure instead of a flexural failure for distance between loads of 3 m, as clearly evidenced in Figure 13b.

To account for uncertainty, a more detailed analysis was performed on the same model. Specifically, uncertainties can be of epistemic or aleatory nature (fib Model Code for Concrete Structures 2010, 2013; Miluccio, Losanno, Parisi, & Cosenza, 2021). In this work aleatory uncertainties were considered in terms of material properties, while epistemic uncertainties, related to the lack of knowledge in the definition of the model (also known as model uncertainty) were disregarded, according to other studies (e.g. Miluccio et al., 2021). Concerning the material properties $f_c, f_{y,8}, f_{y,14}, f_{y,28}$, they were assumed as random variables with a normal distribution and standard deviation of 6.31 MPa for concrete strength f_c, 39.53 MPa; 36.00 and 44.36 MPa respectively for the steel yield strengths of longitudinal and transverse reinforcements: $f_{y,8}, f_{y,14}, f_{y,28}$. It is worth noting that, due to the limited number of available experimental tests on materials, the selection of one specific distribution is not straightforward.

Actually, taking as an example the compressive strength of concrete, it can be observed from the Q-Q plots (Figure 14) for normal and lognormal distributions that both represent reasonably well the experimental data, with a slight better fitting of normal distribution. Applying for the same case the Shapiro-Wilk test for normality, it can be observed that for both distributions the null hypothesis cannot be rejected, stating that both normal and lognormal distributions can be reasonably adopted for the obtained data, with a slightly larger *p* value for the case of normal distribution. The comparison of the two distributions with the histograms of the underlying

data (Figure 15) show that the difference between normal and lognormal distribution is not particularly relevant at this stage of the research. Based on these considerations, a normal distribution for the material properties has been adopted.

The analysis has been carried out with a Monte Carlo approach, running 10'000 simulations for each selected value of distance between loads (i.e. 2, 3, 4, 5, 6 m). For the case of distance between loads equal to 3 m, a further analysis was performed considering the shifted case previously described (i.e. a shift in the diagonal bar Pos 7 of 5 cm toward the supports). The results obtained are depicted in Figure 16a, indicating the values of flexural (in black) and shear (in red) failure loads for each realization and for each value of selected distance. The mean value is depicted as a large dot and the standard deviation is indicated as a bar above and below the mean point. For the case of distance equal to 3 m, two distributions of failure load are found for shear failure, indicated as N and S respectively, for nominal and shifted position of the diagonal bar Pos 7.

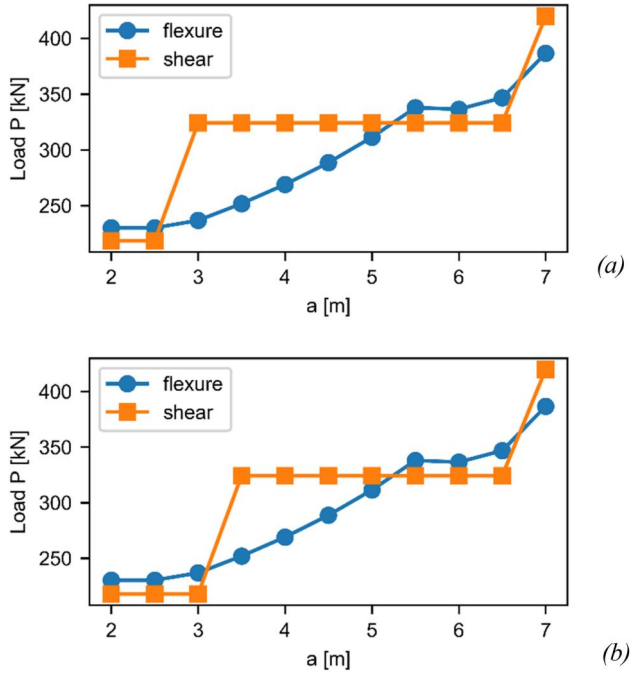

Figure 13. Load P leading to flexural and shear failure for different values of distance a between the forces: (a) for the nominal position of the inclined bars; (b) for a shift of 5 cm of the diagonal bar Pos 7 toward the supports (shifted case).

In Figure 16b, as an example for distance equal to 3 m, it is possible to see the histogram of the realizations (with filled color) and a normal distribution with computed mean and standard deviation. Finally, Table 3 reports the probability of having shear failure (i.e. probability that the load leading to shear failure is lower than the load leading to flexural failure) as a function of the distance between the forces. Based on these results, the distance between the forces of the test setup was selected equal to 4 m, in order to minimize the probability of having shear failure. In the subsequent paragraph, this value will be adopted for more refined analyses in order to estimate the other parameters necessary for the final design of the experimental setup.

3.3. Predictive FE numerical simulations

A finite element model of the central beam has been developed and static non-linear analysis has been performed. The Open System for Earthquake Engineering (OpenSees) framework (McKenna, Scott, & Fenves, 2010) was adopted with the pre- and post- processor Scientific ToolKit for OpenSees (STKO), Petracca, Candeloro, and Camata (2017). Noting how these preliminary analyses intend to support the design of the test set-up rather than to simulate the test itself, a simplified modeling approach has been chosen. Indeed, a simplified modeling approach permits performing analyses that are meant to be carried out without the knowledge of all the parameters necessary for a more refined approach. In the future, when the necessary parameters will be available

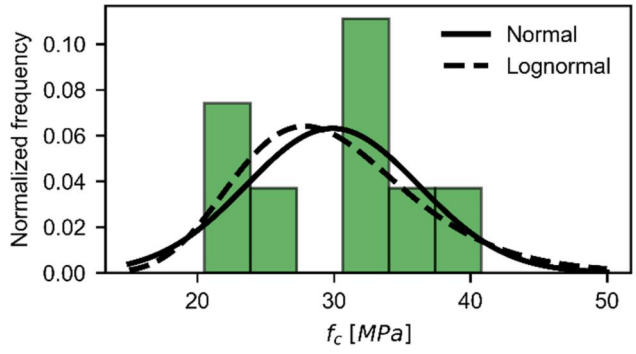

Figure 15. Comparison between normal and lognormal distributions superimposed on the histogram of experimental results for concrete compressive strength.

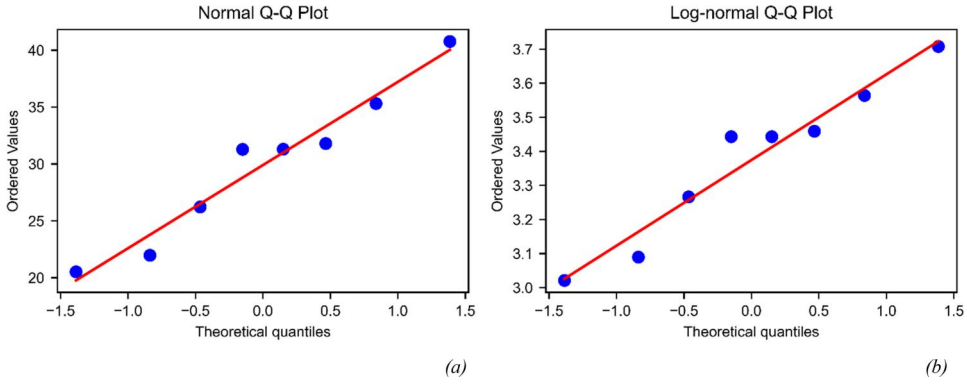

Figure 14. Q-Q plots for: a) normal distribution; b) lognormal distribution.

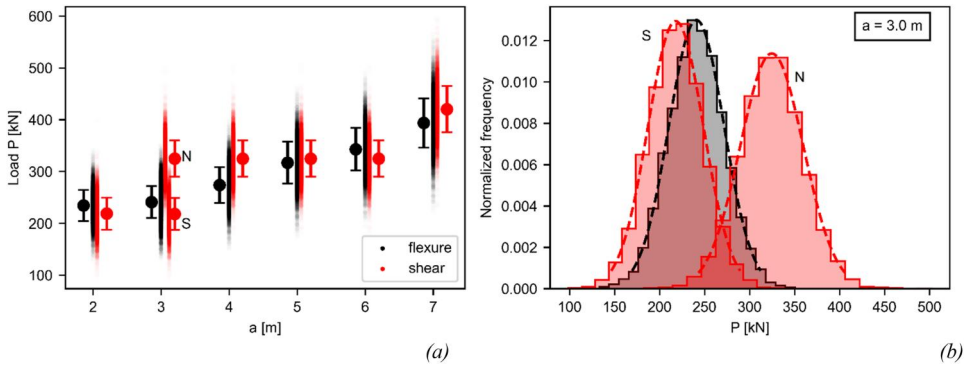

Figure 16. Results obtained from Monte Carlo simulation on analytical model: (a) values of flexural (in black) and shear (in red) failure loads for each realization and for each value of selected distance between forces. The mean value is indicated with a large dot and the standard deviation is indicated as a vertical bar; (b) histogram of the realizations (with filled color) and a normal distribution with computed mean and standard deviation for the case $a = 3.0$ m (N and S indicate, respectively, nominal and shifted position of the diagonal bar Pos 7).

Table 3. Probability of shear failure.

a [m]	Prob(V < M) [%]
2.0	63.98
3.0	0.70
3.0*	70.29
4.0	8.22
5.0	42.43
6.0	67.80
7.0	22.43

*considering a 5 cm shift of the diagonal bar.

in the post-test phase, more refined finite element analyses will be performed. In particular, advanced non-linear models will be adopted in order to properly represent both the flexural and shear behavior of T-cross section beams.

The numerical models were realized using a distributed plasticity approach by means of force-based nonlinear elements with fiber discretization of cross sections (Spacone, Filippou, & Taucer, 1996) (Scott et al., 2008; Spacone et al., 1996; Taucer et al., 1991). The Gauss-Lobatto scheme with 5 integration points was selected for numerical integration. Since the reinforcement layout changes along the longitudinal axes of the beam (see Figure 6), each integration point is characterized by the same concrete geometry and different layout of longitudinal reinforcement. State that in OpenSees only one cross-section can be selected for all integration points for standard integration algorithms like Gauss-Lobatto scheme, in this work the position and the weight of the integration points were specified manually, for each beam element. The model was discretized with 4 beam elements, that is the minimum number required to simulate a four-point bending scheme. As it is well known, no further discretization is necessary for force-based beam-column elements. The applied constraints simulate the designed experimental setup with a roller in the left side, as visible in Figure 17. In a first phase, a distributed load simulating the self-weight was applied increasing the load in 10 steps. Then, maintaining constant the applied distributed load, the two vertical forces with a distance of 4 m were applied; a displacement control algorithm was employed controlling the vertical degree of freedom of the midpoint node and computing the corresponding load multiplier.

Regarding material constitutive laws, concrete was modeled with a simple Kent-Park model, concrete tensile strength is disregarded and reinforcement steel was modeled with an elastic-plastic law with hardening. The mean values of material properties adopted in the analysis are reported in Table 4. It is worth mentioning that elastic modulus of reinforcement steel was measured only on tests of bars with 14 mm of diameter. Therefore the same value is adopted for bars with 28 mm of diameter. The hardening ratio b of steel constitutive law, defined as the ratio between the hardening stiffness and the elastic modulus, was computed starting from the experimentally values obtained for yield and ultimate strength, together with the manual measurement of strain at peak stress A_{gt} according to the following relation:

$$b = \frac{f_t - f_y}{A_{gt} - \varepsilon_y} \cdot \frac{1}{E} \tag{1}$$

Since the adopted fiber-based modeling is not able to take into account shear failure, shear strength was estimated by the analytical truss model adopted also for the preliminary design phase. A post-processing check was then carried out at each load step, indicating with a flag when shear failure occurs, corresponding to the attainment of the yield strength for stirrups. The force-midpoint displacement curve obtained by static non-linear analysis is depicted in Figure 18, The red circle indicates the attainment of the shear failure: as expected from the results of the previous analysis, the shear failure takes place after yielding phase of the longitudinal bars, occurring at about 20 mm of midpoint displacement and about 530 kN of force. The peak force is about 700 kN for a corresponding midpoint displacement of about 520 mm.

After the peak, the force-displacement curve exhibits a softening branch due to the crushing of concrete in the flange. Figure 19 shows the compressive stresses in the upper zone of the beam in four different points of the force-displacement curve, respectively at longitudinal bar yielding (A), at the incipient failure of upper concrete cover (B), at the peak load (C) and in the softening branch (D). After the peak stress attainment, observing the compressive stresses in the fibers immediately adjacent to the point of force application, it can be seen that there is a sudden lowering of the neutral axis until reaching the upper edge of the web of the beam

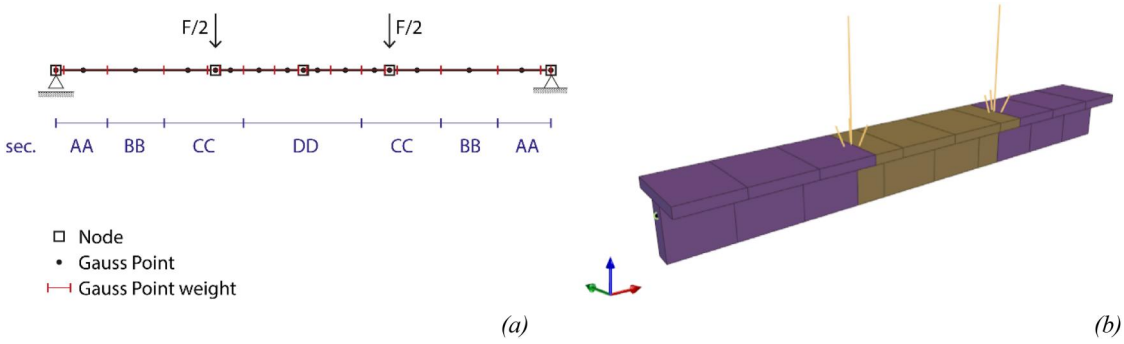

Figure 17. FE model: (a) supports and load scheme, discretization, integration points and cross sections used; (b) 3D view.

(compare the fibers in the zoomed zones in Figure 19c,d). After yielding, the curvature shows a localization in the two regions close to the force application, where the bending moment is almost maximum but the reinforcement area is smaller than that present in the central zone, see Figure 20.

An important goal of the proposed numerical simulation is the estimation of the horizontal displacement and the rotations at the support regions, in order to correctly design the experimental setup and avoid possible contacts between the supporting elements and the beam for the expected rotations before the collapse of the beam under testing. Figure 21 shows the contour of the horizontal displacements at the end of the analysis. In the same figure it is possible to observe the rotation attained in support nodes, equal to about 0.15 radiants. In the left roller, the horizontal displacement (due to elongation of beam generated by the shifted position of the neutral axis respect to the center of gravity of the T-shaped cross section) is about 77 mm. The bottom fiber is located at about 780 mm from the center of gravitiy of the cross section and the horizontal displacement in the left roller can be estimated of about 315 mm, obtained as the x-displacement of the left node (equal to 77.4 mm) plus the sum of the x-displacements (117.8 mm each) of the bottom edge of the beam due to the end nodes rotations.

In order to take the uncertainties in the parameter's estimation into account, Monte Carlo's analyses have been performed considering the eight parameters reported in Table 5 as random variables, while all other characteristics were treated as fully deterministic. Concerning reinforcing steel, since only two tests were performed for bars with 28 mm of diameter, the coefficient of variation (COV) for yield strength (f_y) and hardening parameter (b) are assumed to be the same of those used for the reinforcement with a diameter of 14 mm. The standard deviation of hardening parameter b, defined by Equation (1), was approximately estimated by linearizing the function to the first order and applying the usual uncertainty propagation rule assuming all variables uncorrelated except for f_y and f_t:

Table 4. Mean values of material properties adopted in the numerical analyses.

Material	Property	Value
Concrete	Compressive strength f_c	29.89 MPa
	Strain at peak stress ε_{c0}	0.002
	Ultimate strain ε_{cu}	0.006
Reinforcement ϕ14	Elastic modulus $E_{\phi 14}$	216,722 MPa
	Yield strength $f_{y,\phi 14}$	381.98 MPa
	Ultimate strength $f_{t,\phi 14}$	520 MPa
	Ultimate strain $A_{gt,\phi 14}$	27.42 %
	Hardening ratio $b_{\phi 14}$	0.0023
Reinforcement ϕ28,	Elastic modulus $E_{\phi 28}$	216,722 MPa
	Yield strength $f_{y,\phi 28}$	310.8 MPa
	Ultimate strength $f_{t,\phi 28}$	435 MPa
	Ultimate strain $A_{gt,\phi 28}$	25.55 %
	Hardening ratio $b_{\phi 28}$	0.0023

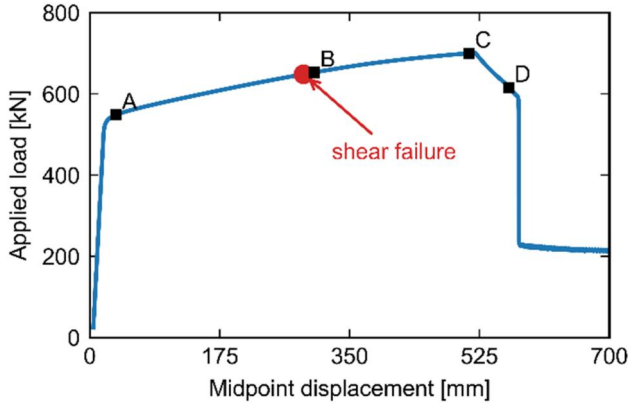

Figure 18. Force-displacement curve obtained by static non-linear analysis. Point A: yielding; point B: incipient failure of upper concrete cover; point C: peak load; point D: softening branch.

where all partial derivatives are computed at the mean value and $\sigma_{f_y f_t}$ is the covariance between f_y and f_t.

Indeed, a preliminary statistical analysis permitted to estimate a significant linear correlation coefficient of 0.92 (with a corresponding p value of 0.025) between these two variables, while it did not permit to find statistically meaningful correlation between the other variables (i.e. E and A_{gt})

$$\sigma_b \approx \sqrt{\left(\frac{\partial b}{\partial f_y}\right)^2 \sigma_{f_y}^2 + \left(\frac{\partial b}{\partial f_t}\right)^2 \sigma_{f_t}^2 + \left(\frac{\partial b}{\partial A_{gt}}\right)^2 \sigma_{A_{gt}}^2 + \left(\frac{\partial b}{\partial E}\right)^2 \sigma_E^2 + \frac{\partial b}{\partial f_y}\frac{\partial b}{\partial f_t}\sigma_{f_y f_t}} \quad (2)$$

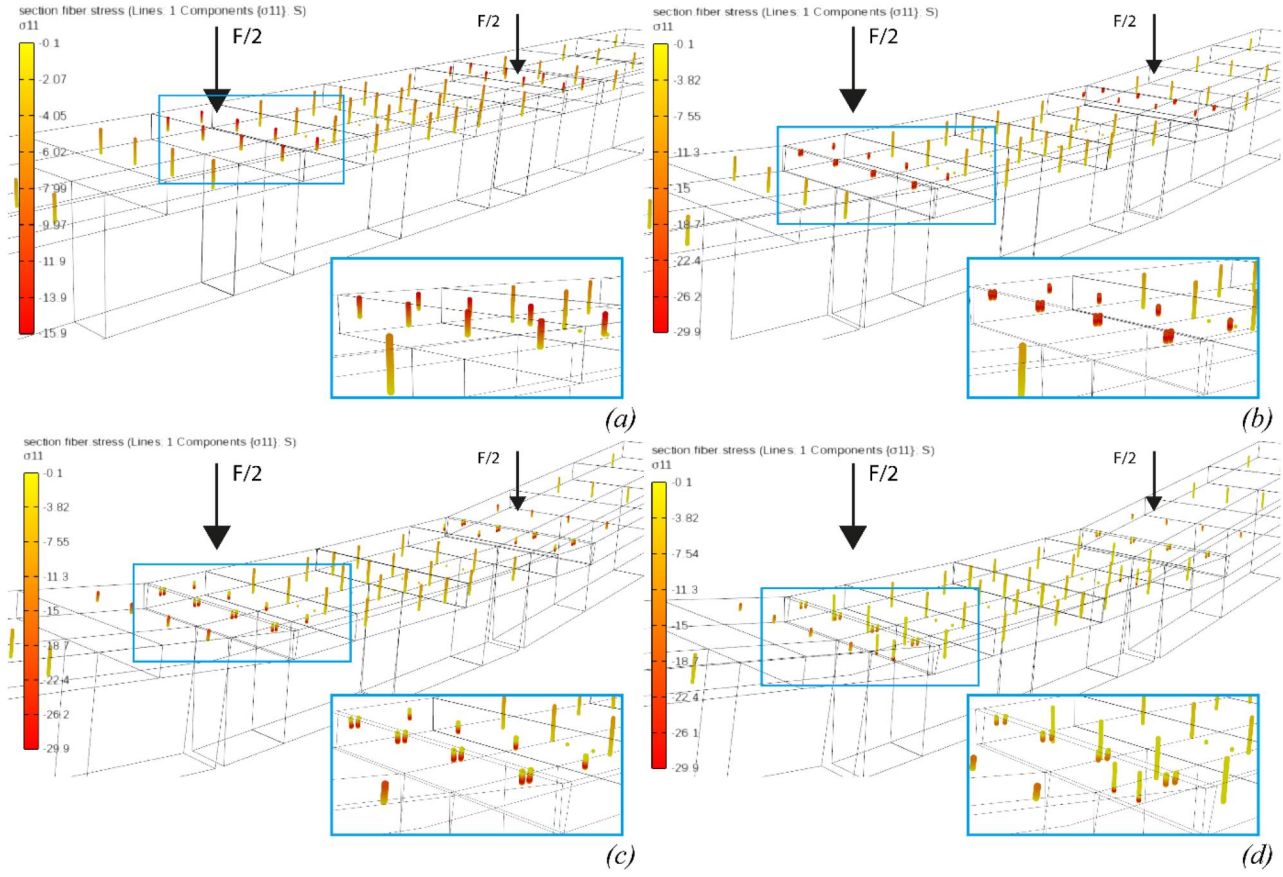

Figure 19. Distribution of concrete stresses in the Central portion of the beam for different stages of the analysis: (a) yielding corresponding to point a in Figure 18; (b) incipient failure of upper concrete cover corresponding to point B in Figure 18; (c) peak load corresponding to point C in Figure 18; softening branch corresponding to point D in Figure 18.

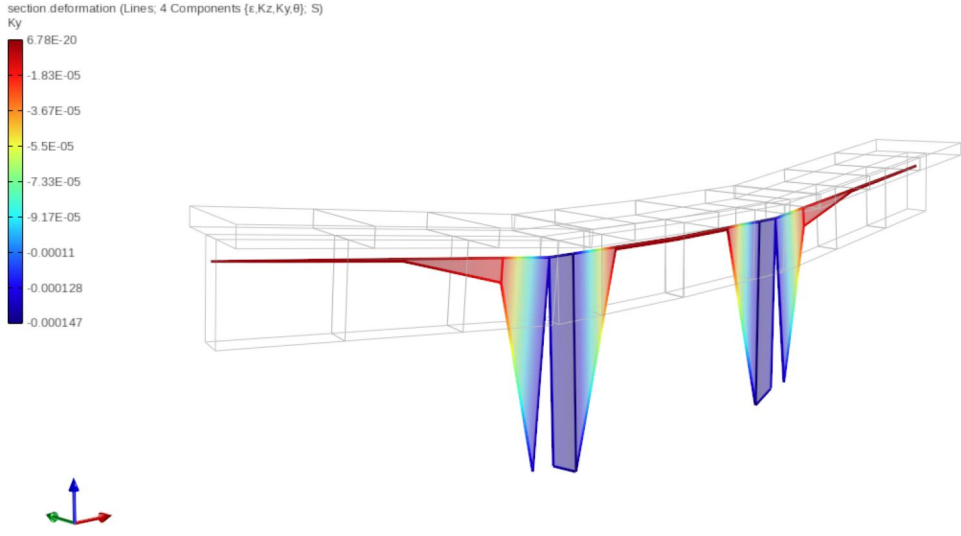

Figure 20. Curvature distribution (mm^{-1}) corresponding to a midpoint displacement of about 520 mm.

mainly due to the low number of tests. For this reason, these parameters are assumed to be independent (i.e. their respective covariances are zero). Future experimental tests will involve more reinforcement bars extracted after full-scale beam tests, providing additional data to improve the robustness of statistical parameters and assumptions, enabling better correlation estimates. As the hardening ratio b must be positive, a lognormal distribution was assumed for this parameter. Finally, since no experimental data was available for the ultimate strain ε_{cu} of concrete, a medium-high value COV = 0.25 was assumed.

In the Monte Carlo simulation, a total of 1000 analyses have been performed extracting for each of the eight parameters a value according to their respective assumed distributions. For each set of parameters extracted, the corresponding numerical model is run in OpenSees. The distribution

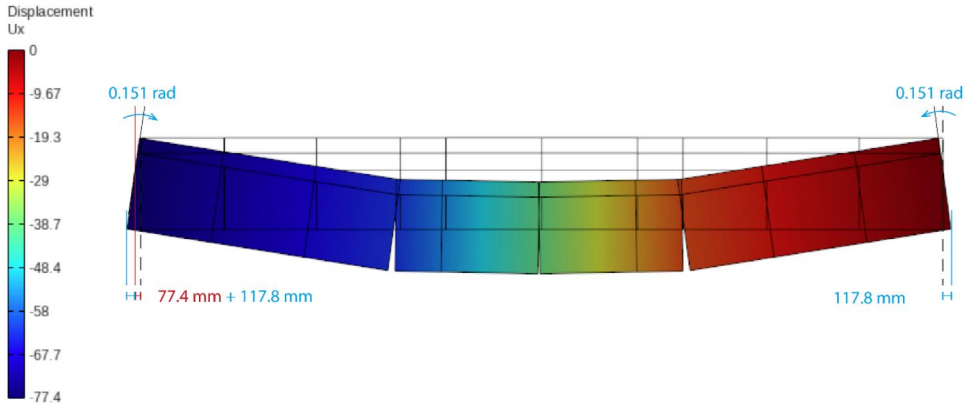

Figure 21. Contour of x-displacement of the beam element at the end of analysis and displacements at bottom side.

Table 5. Distribution parameters of mechanical properties assumed as random variables.

Material	Parameter	Unit	Distribution	Mean	Std. dev.	COV
Concrete	f_c	MPa	N	29.89	6.31	0.21
	ε_{cu}	–	N	0.006	0.0015	0.25
Reinforcement ϕ14	$E_{\phi 14}$	MPa	N	216,722	28,752	0.133
	$f_{y,\phi 14}$	MPa	N	381.98	44.36	0.116
	$b_{\phi 14}$	–	LN	0.002346	0.001692	0.721
Reinforcement ϕ28	$E_{\phi 28}$	MPa	N	216,722	28,752	0.133
	$f_{y,\phi 28}$	MPa	N	310.80	36.00	0.116
	$b_{\phi 28}$	–	LN	0.002256	0.001627	0.721

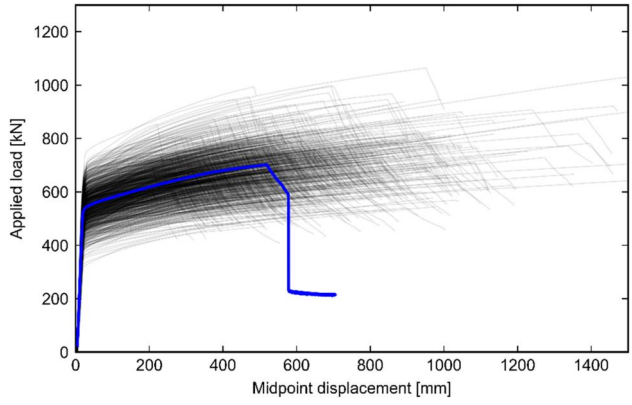

Figure 22. Force-displacement curve obtained by Monte Carlo simulation: blue curve is the one corresponding to mean values of parameters.

obtained from the extracted values of parameters fairly matches the assumed distributions, supporting the validity of the obtained outcomes. The target displacement of all analyses was set equal to 1500 mm and an adaptive step algorithm was employed in order to overcome convergence issues, reducing or increasing the steps in dependence to the number of iterations performed in the previous step; in particular the step can be reduced up to 1/1000 of the original tentative size of 1 mm. In order to reduce computational time, particularly significant in the analyses stage where high non-linearity and difficulties of convergence can arise, the analysis was performed step by step by monitoring the load multiplier at each step: when the load multiplier drops down more than 15% respect the peak force, the analysis is interrupted.

In order to reduce the computational effort, only the global force-displacement curves were saved during the analyses. To process the results, a cleaning phase, eliminating nonrealistic points achieved numerically, is necessary. For each curve, the yielding point is computed as the point for which secant stiffness changes from the initial stiffness more than 5%, peak point is defined as the point with maximum force, while ultimate displacement is defined as the point meeting the first of the following criteria: (i) the point corresponding to a reduction of 15% of the peak load; (ii) the last point in the curve if lower than peak point (due to numerical errors it may occur for some curves that the last point is higher than the peak point). Finally, the possibility of reaching a shear failure is computed in the post-processing phase as described previously for each curve, by selecting the yield strength of the stirrups $f_{y,8}$ randomly from the assumed normal distribution, with mean value of 310.6 MPa and standard deviation equal to 6.31 MPa.

The results obtained in terms of load-displacement curves are depicted in Figure 22 where the blue curve corresponds to the mean values of the parameters (i.e. the one reported in Figure 18). It is possible to see that, due to the large COV value of some parameters (especially the hardening ratio), the response is extremely scattered, in particular with reference to ultimate displacement (ranging from about 200 mm to more than 1500 mm). The results in terms of distributions obtained for the output values, i.e. initial stiffness (K), displacement and force at yielding (F_y and x_y), maximum force and corresponding displacement ($F_{\max}$ and $x_{\max}$), ultimate displacement (x_u) are depicted in Figure 23. The corresponding mean standard deviation values (represented in Figure 23, respectively, with solid and dashed lines) are reported in Table 6. The very large scatter of the results of peak and ultimate displacement, with corresponding COV values larger than 0.3, is evident. The other quantities are obtained with COV values about 0.15 or lower.

Based on these results, the probability of reaching a maximum load exceeding 1000 kN (the sum of the maximum

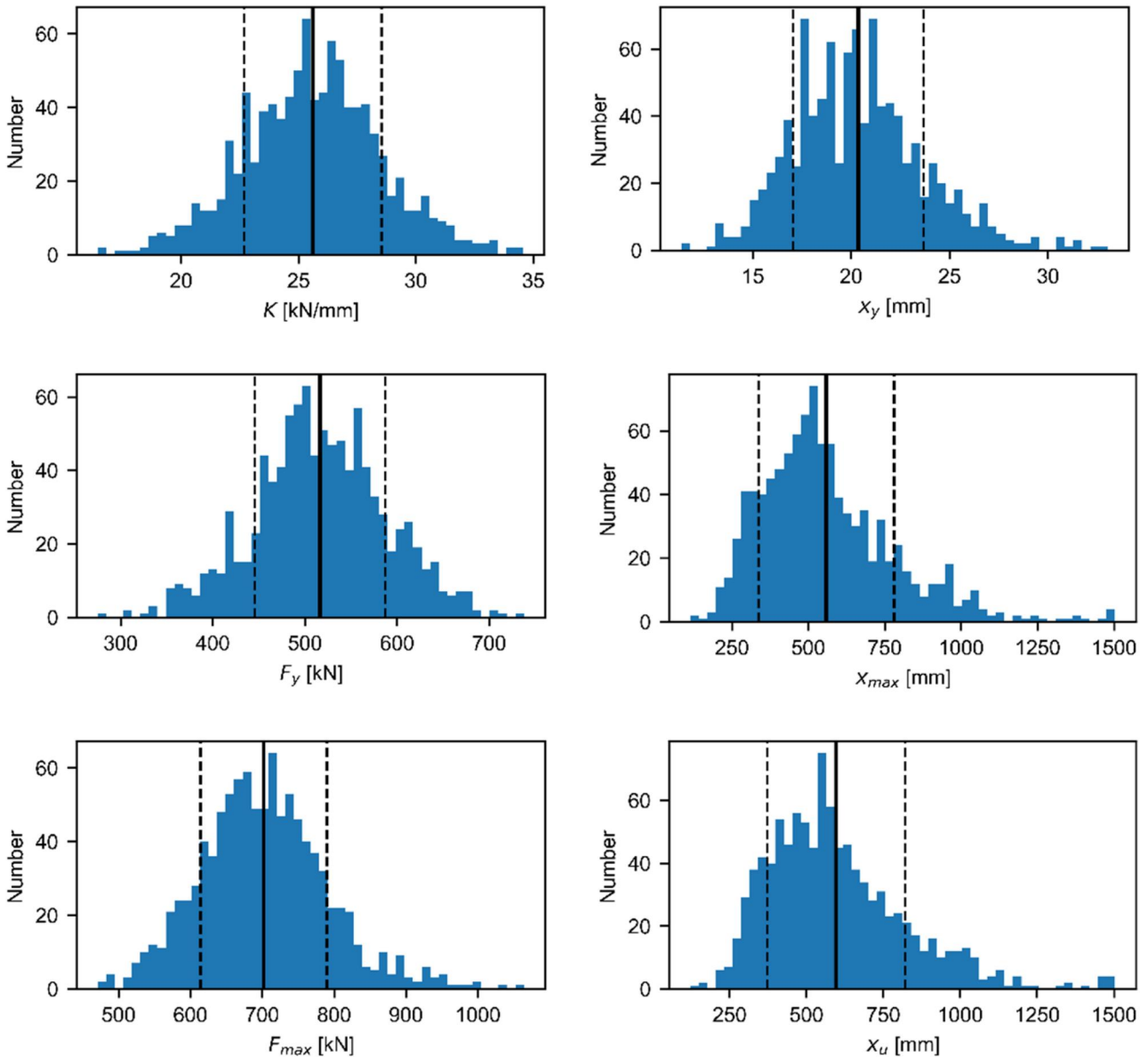

Figure 23. Results of Monte Carlo analyses: histograms of output values obtained from load-displacement curves. The vertical solid black line represents the mean value while vertical dashed black lines represent mean ± one standard deviation.

Table 6. Results from Monte Carlo analyses: distribution parameters of key output variables.

Output parameter	Symbol	Unit	Mean	Std. dev.	COV
Elastic stiffness	K	kN/mm	25.61	2.93	0.114
Yield force	F_y	kN	516.29	70.74	0.137
Yield displacement	x_y	mm	20.36	3.32	0.163
Max force	F_{max}	kN	701.97	88.09	0.125
Displacement at max force	x_{max}	mm	558.63	221.53	0.397
Ultimate displacement	x_u	mm	595.84	224.22	0.376

load from the two MTS servo-hydraulic actuators to be adopted in the experimental design) is about 0.2%, which can be considered a sufficiently low probability, so allowing to confirm the suitability of the selected test facilities. Conversely, the stroke of the MTS servo-hydraulic actuators equal to 450 mm proves to be inadequate to induce failure in the girder that occurs for displacement values of approximately 600 mm when adopting mean values of material parameters. To address the setup limitation, a custom solution was designed, incorporating a special removable support for the reaction frames. This system can be removed once the actuator stroke is completed, enabling a maximum mid-span deflection of 900 mm. The probability of reaching this specified deflection is estimated being about 10.4%, which is considered reasonably low and falls within acceptable limits for the research objectives.

Finally, the probability of occurrence of shear failure before yielding of longitudinal steel reinforcement is about 3.2% (pure shear failure), while the probability of having a shear failure after yielding but before the attainment of the flexural peak load is of 66.1%; therefore, the probability of having a pure flexural failure is of about 31%. Being the probability of shear failure (after yielding of longitudinal bars) rather high, the test equipment will be integrated with a DIC (Digital Image Correlation) system that will allow for a thorough monitoring of the crack pattern evolution, fundamental to interpret the actual failure mode.

3.4. Setup for full scale bending test of sampled girders

The final experimental setup for the four points bending test confirms the one defined by the preliminary design. The test scheme is symmetric and consists of a simply supported girder with two vertical loading points placed at a distance of 2 m from the centerline (i.e. the distance between the load points is equal to 4 m). The results of advanced FE simulation discussed before allowed to define the limit values of: maximum force required by the actuators at each loading point P; maximum mid-span deflection δ_{Vmax}; maximum lateral displacement of the sliding support δ_{Hmax}; maximum end rotation of supports β_{max}. Based on those values, a specific test setup equipment was designed to carry out the full scale four point bending test. The setup equipment is represented in Figure 24 and consists of the components described below:

- Two specifically designed steel reaction frames equipped with a 500 kN MTS servo-hydraulic actuator each, with a maximum stroke equal to 450 mm. The maximum applicable total load is therefore equal to $P = 1000$ kN. Each steel frame is anchored to the strong floor of the laboratory by means of four Dywidag bars. The MTS actuators are equipped with spherical hinges at both extremities.
- Two 150 mm x150 mm steel box beams are used to distribute the local action applied by the actuators on the extrados of the girder slab. The transversal elements are fixed to both actuator terminal hinge and RC slab. Connection with RC slab is realized by means of four passing bars and counter plate.
- Four RC removable supports for the metal frames. These elements can be removed at a certain step during the test to recover the actuator stroke, allowing to prescribe higher values of mid-span deflection to the girder. Removing the removable support elements in subsequent steps, the maximum deflection attainable during the test is equal to $\delta_{Vmax} = 900$mm (twice the basic stroke of the MTS actuator);
- Two RC basements for the end supports of the girder. Each RC basement is anchored to the strong floor of the laboratory by means of four Dywidag bars;
- The hinge support (Figure 25a) is realized by means of two machined thick steel plates with a ground steel cylinder placed between them. The cylinder is welded to the base plate while the upper plate is carved (crescent-shaped hollow) so as to keep the cylinder in position but allowing the upper plate rotation. Sliding is prevented by the anchoring of the lower plate to the RC basement. The girder rests directly on the upper machined plate by interposing a 20mm thick neoprene layer. The maximum end rotation allowed by the device is equal to β_{max}= 12 degrees;
- The sliding support (Figure 25b) is realized with a double steel plate system. The first (upper) plate system is similar to that adopted for the hinged constraint, to allow for the beam rotation. The second one is required to allow the horizontal displacement, by a series of steel rollers interposed between the base plate of the hinge system and a sliding plate anchored to the RC basement. The maximum lateral displacement allowed by the

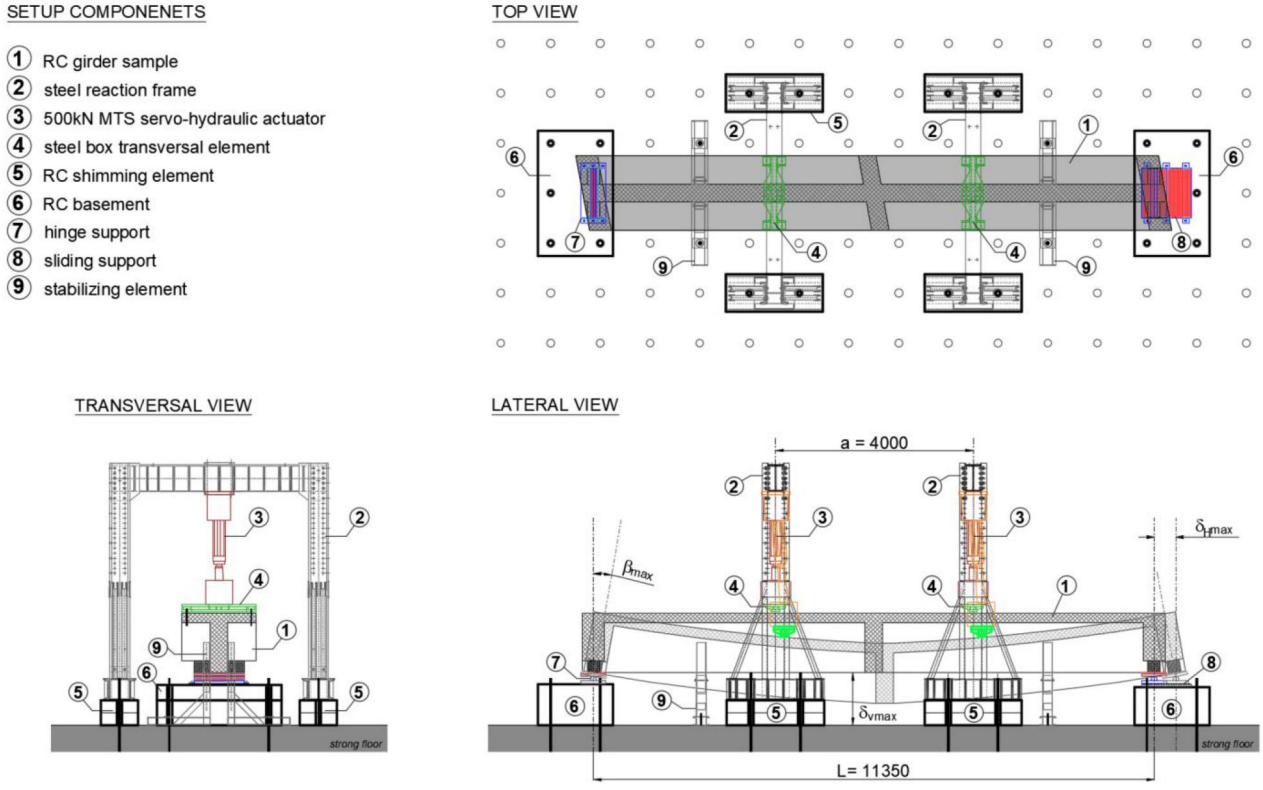

Figure 24. Global view of the designed experimental setup. In the lateral view of the setup, deformed configuration of the girder is superimposed to the undeformed one.

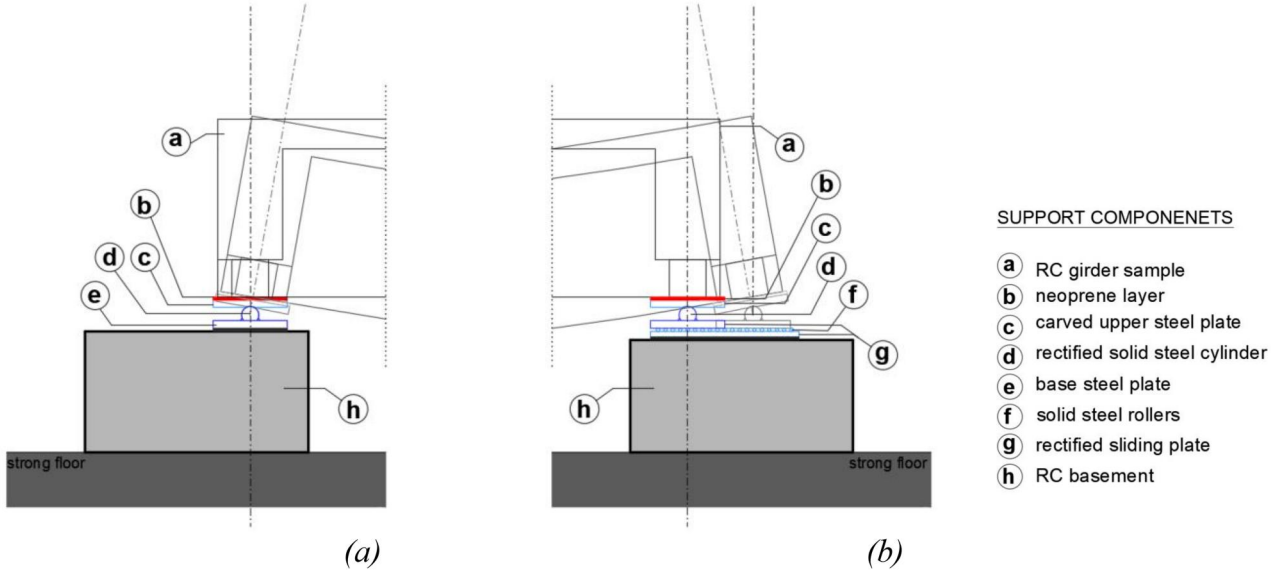

Figure 25. Details/zoom of support system: (a) hinge support and (b) sliding support.

system is $\delta_{Hmax} = 500\,mm$ while the maximum end rotation is $\beta_{max} = 12$ degrees.

All the contact surfaces of the components of the support devices that rotate or slide are machined to limit friction phenomena. The entire setup equipment is specifically designed to reach the ultimate displacement capacity of the bridge girder. Indeed, in bending tests, the compatibility of the actuator stroke with the girder ultimate displacement capacity is a key aspect as demonstrated, for example, by recent experimental research on post-tensioned concrete bridge girders carried out by Losanno et al. (2024). Within the proposed setup, removable supports are provided to recover the actuator stroke according to a specifically designed test procedure. This experimental procedure plans to stop the test at a level of ductility demand compatible with the stroke of the actuators. Once the test has been stopped, the girder is pulled down using two couple of rigid steel beams, placed near the load application points and rigidly anchored to the strong floor.

The anchoring system is equipped with load cells to measure the forces applied to the girder during the transient phase necessary for the recovery of the actuator stroke. After the recovery of the stroke, the actuators are brought back to the target load level and the temporary blocking system removed. It is worth noting that the recovery of the actuator stroke does not impact on the displacement measurement system which remains active recording the girder deformation. Moreover, for high level of ductility demand the experimental procedure could involve loading/unloading cycles aimed, for example, at evaluating the dynamic behavior of the girder for increasing level of damage. In this case, the stroke recovery can be easily carried out at the end of an unloading cycle.

4. Conclusions

This paper presents the initial phase of an integrated numerical - experimental research, aiming to contribute to the development of procedures for studying existing bridge infrastructures. The opportunity to study an existing reinforced concrete (RC) bridge built around the 1950s, originally scheduled for demolition, allowed for the design of an experimental testing campaign both on-site and, in a second phase, to be conducted in the laboratory on full-scale elements (mainly the bridge beams) degraded naturally by external agents.

This research thus has a dual objective. Firstly, it aims to provide reliable indications on the actual effectiveness of the main on-site tests and investigations currently available, compared to the investigations and tests to be conducted in the laboratory both before and after the elements' failure tests. In particular, the effectiveness of on-site investigations in determining the mechanical characteristics of materials, detecting construction details, and predicting the actual degradation state of the elements, especially the level of corrosion, should be evaluated.

Furthermore, the full scale failure tests to be conducted in laboratory on the four beams of the deck will allow for an effective comparative evaluation in terms of failure modes and element strengths depending on the different degradation levels of the two external beams of the deck compared to the internal ones. Up to now, following an extensive on-site survey campaign of the bridge, verifying its various phases and graphically presenting the essential elements, the laboratory testing method has been designed to bring the beams to a flexural failure. Large forces and especially large displacements are expected, and then the experimental setup must be carefully designed in order to reach the full collapse of the beams.

For this purpose, two different modeling approaches were adopted, the first utilizing the mean material parameters and the geometric survey data and construction details obtained from the tests. Subsequently, a Monte Carlo analysis was conducted to assess the effect of uncertainties in these parameters on the outcomes of the failure test, leading to the final design of the test setup.

Acknowledgements

The studies were carried out as part of two research projects: the first is envisaged by the Agreement between the High Council of Public Works (CSLLPP) and the ReLUIS Consortium implementing Ministerial Decree 578/2020 and Ministerial Decree 240/2022 (the contents of this paper represent the authors' ideas and do not necessarily correspond to the official opinion and policies of CSLLPP). The second activity is carried out within the RETURN Extended Partnership and received funding from the European Union Next-GenerationEU (National Recovery and Resilience Plan – NRRP, Mission 4, Component 2, Investment 1.3 – D.D. 1243 2/8/2022, PE0000005). The kind support of the Padua Province is finally acknowledged.

Disclosure statement

No potential conflict of interest was reported by the author(s).

References

ASCE. (2021). 2021 report card for America's infrastructures.

Bagge, N., Blanksvärd, T., Carolin, A., Sas, G., Elfgren, L., Nilimaa, J., & Tu, Y. (2015). *Loading to failure of a 55 year old prestressed concrete bridge*. IABSE Workshop Helsinki - Safety, Robustness and Condition Assessment of Structures, 130–137. doi:10.2749/222137815815622780

Bagge, N., Popescu, C., & Elfgren, L. (2018). Failure tests on concrete bridges: Have we learnt the lessons? *Structure and Infrastructure Engineering*, *14*(3), 292–319. doi:10.1080/15732479.2017.1350985

Bencivenga, P., Buratti, G., Cosentino, A., De Matteis, G., Morelli, F., Salvatore, W., & Zizi, M. (2022). Evolution of design traffic loads for Italian road bridges. *Lecture Notes in Civil Engineering*, *200*, 1351–1358.

Calvi, G. M., Moratti, M., O'Reilly, G. J., Scattarreggia, N., Monteiro, R., Malomo, D., … Pinho, R. (2019). Once upon a time in Italy: The tale of the Morandi. *Structural Engineering International*, *29*(2), 198–217. doi:10.1080/10168664.2018.1558033

CEN. (2015). EN1992-1-1 - Eurocode 2: Design of concrete structures - Part 1-1: General rules and rules for buildings.

Cheilakou, E., Theodorakeas, P., Koui, M., Moustakidis, S., & Zeris, K. (2013). *Application of Ground Penetrating Radar (GPR) as a diagnostic technique in concrete bridges inspection*. NDE for Safety/Defektoskopie 2012, 42nd International Conference, Oct 30 - Nov 1, 2012, Seč, Czech Republic.

Cosenza, E., & Losanno, D. (2021). Assessment of existing reinforced-concrete bridges under road-traffic loads according to the new Italian guidelines. *Structural Concrete*, *22*(5), 2868–2881. doi:10.1002/suco.202100147

Deng, L., Wang, W., & Yu, Y. (2016). State-of-the-art review on the causes and mechanisms of bridge collapse. *Journal of Performance of Constructed Facilities*, *30*(2), 04015005-1–13. doi:10.1061/(ASCE)CF.1943-5509.0000731

Di Carlo, F., Talledo, D. A., Berto, L., Isabella, P., Meda, A., Rinaldi, Z., & Saetta, A. (2023). A methodology for the evaluation of morphology-based constitutive laws of corroded steel rebars. *Compdyn*.

Eder, R. W., Miller, R. A., Baseheart, T. M., & Swanson, J. A. (2005). Testing of two 50-year-old precast post-tensioned concrete bridge girders. *PCI Journal*, *50*(3), 90–95. doi:10.15554/pcij.05012005.90.95

fib Model Code for Concrete Structures 2010. (2013). Lausanne

Halsey, J. T., & Miller, R. (1996). Destructive testing of two forty-year-old prestressed concrete bridge beams. *PCI Journal*, *41*(5), 84–93. doi:10.15554/pcij.09011996.84.93

Jeon, C. H., Sim, C., & Shim, C. S. (2021). The effect of wire rupture on flexural behavior of 45-year-old post-tensioned concrete bridge girders. *Engineering Structures*, *245*, 112842. doi:10.1016/j.engstruct.2021.112842

Jiang, H., Mo, F., Chen, Z., Wu, J., Fang, H., Fang, Z., … Xu, Z. (2023). Full-scale experimental study of shear and flexural behavior of 16-m retired reinforced concrete t-beams. *Buildings*, *13*(8), 2075. 2023doi:10.3390/buildings13082075

Lantsoght, E. O. L., Yang, Y., van der Veen, C., de Boer, A., & Hordijk, D. A. (2016). Ruytenschildt Bridge: Field and laboratory testing. *Engineering Structures*, *128*, 111–123. doi:10.1016/j.engstruct.2016.09.029

Liu, J., & Jia, Y. (2019). Destructive testing of twenty-year-old prestressed concrete bridge beams in freezing-thawing region. *Stavební obzor - Civil Engineering Journal*, *28*(3), 344–356. doi:10.14311/CEJ.2019.03.0028

Losanno, D., Galano, S., Parisi, F., Pecce, M. R., & Cosenza, E. (2024). Experimental investigation on nonlinear flexural behavior of post-tensioned concrete bridge girders with different grouting conditions and prestress levels. *Journal of Bridge Engineering*, *29*(3), 04023121. doi:10.1061/JBENF2.BEENG-6466

McKenna, F., Scott, M. H., & Fenves, G. L. (2010). Nonlinear finite-element analysis software architecture using object composition. *Journal of Computing in Civil Engineering*, *24*(1), 95–107. doi:10.1061/(ASCE)CP.1943-5487.0000002

Miller, R. A., Aktan, A. E., & Shahrooz, B. M. (1994). Destructive testing of decommissioned concrete slab bridge. *Journal of Structural Engineering*, *120*(7), 2176–2198. doi:10.1061/(ASCE)0733-9445(1994)120:7(2176)

Miluccio, G., Losanno, D., Parisi, F., & Cosenza, E. (2021). Traffic-load fragility models for prestressed concrete girder decks of existing Italian highway bridges. *Engineering Structures*, *249*, 113367. doi:10.1016/j.engstruct.2021.113367

MIT. (2020). Ministerial Decree 578 on 17.12.2020. Guidelines for risk classification, safety assessment and structural health monitoring of existing bridges. Italy (in Italian).

MIT. (2018). *D.M. 17/01/2018. Technical code for constructions*. Rome, Italy: Italian Ministry of Infrastructures and Transportation (in Italian).

MIT. (2019). *Circolare n.7 C.S.LL.PP. 21/01/2019. Commentary on technical code for constructions*. Rome, Italy: Italian Ministry of Infrastructures and Transportation (in Italian).

Papé, T. M., & Melchers, R. E. (2011). The effects of corrosion on 45-year-old pre-stressed concrete bridge beams. *Structure and Infrastructure Engineering*, *7*(1-2), 101–108. doi:10.1080/15732471003588411

Pessiki, S., Kaczinski, M., & Wescott, H. H. (1996). Evaluation of effective prestress force in 28-year-old prestressed concrete bridge beams. *PCI Journal*, *41*(6), 78–89. doi:10.15554/pcij.11011996.78.89

Petracca, M., Candeloro, F., & Camata, G. (2017). *STKO user manual*. Pescara: ASDEA Software Technology.

Rogers, R. A., Wotherspoon, L., Scott, A., & Ingham, J. M. (2012). Residual strength assessment and destructive testing of decommissioned concrete bridge beams with corroded pretensioned reinforcement. *PCI Journal*, *57*(3), 100–118. doi:10.15554/pcij.06012012.100.118

Savino, P., Tondolo, F., Sabia, D., Quattrone, A., Biondini, F., Rosati, G., Anghileri, M., & Chiaia, B. (2023). Large-scale experimental static testing on 50-year-old prestressed concrete bridge girders. *Applied Sciences*, *13*(2), 834. doi:10.3390/app13020834

Scott, M. H., Fenves, G. L., McKenna, F., & Filippou, F. C. (2008). Software patterns for nonlinear beam-column models. *Journal of Structural Engineering, 134*, 562–571.

Shenoy, C. V., & Frantz, G. C. (1991). Structural tests of 27-year-oid prestressed concrete bridge beams. *PCI Journal*, *36*(6), 80–90. doi:10.15554/pcij.09011991.80.90

Spacone, E., Filippou, F. C., & Taucer, F. F. (1996). Fibre beam-column model for non-linear analysis of R/C frames: Part I. Formulation. *Earthquake Engineering Structural Dynamics, 25*, 711–725.

Taucer, F. F., Spacone, E., & Filippou, F. C. (1991). 'A fiber beam-column element for seismic response analysis of reinforced concrete structures', EERC Report 91/17. Earthquake Engineering Research Center, University of California, Berkeley.

Taffe, A., Hillemeier, B., & Walther, A. (2010). Condition assessment of a 45-year old prestressed concrete bridge using NDT and verification of the results. *E-Journal of Nondestructive Testing*, *15*(10).

Täljsten, B., Nilimaa, J., Blanksvärd, T., & Sas, G. (2011). *Flexural-shear failure of a full scale tested RC bridge strengthened with NSM CFRP*. 5th International Conference on Structural Health Monitoring of Intelligent Infrastructure (SHMII-5), December 11–15, Cancún, México.

Tonelli, D., Rossi, F., Brighenti, F., Verzobio, A., Bonelli, A., & Zonta, D. (2023). Prestressed concrete bridge tested to failure: The Alveo Vecchio viaduct case study. *Journal of Civil Structural Health Monitoring*, *13*(4-5), 873–899. doi:10.1007/s13349-022-00633-w

Wang, J., Tang, S., Zheng, H., Zhou, C., & Zhu, M. (2020). Flexural behavior of a 30-meter full-scale simply supported prestressed concrete box girder. *Applied Sciences*, *10*(9), 3076. doi:10.3390/app10093076

Žnidarič, A., Pakrashi, V., O'Brien, E., & O'Connor, A. (2011). A review of road structure data in six European countries. *Proceedings of the Institution of Civil Engineers - Urban Design and Planning*, *164*(4), 225–232. doi:10.1680/udap.900054